ELSEVIER

Contents lists available at ScienceDirect

Computers in Biology and Medicine

journal homepage: www.elsevier.com/locate/compbiomed





Development of a methodology for *in vitro* and *in silico* simulation of transcatheter aortic valve replacement using 3D-printed valve frames

Xiao Zhao ^a, Oguz Can Eren ^{b, *}, Anthony Molyneux ^c, Louise Geekie ^{c, *}, Nick Curzen ^{d, *, *}, Neil W. Bressloff ^{f, *}

- a School of Engineering, Faculty of Engineering and Physical Sciences, University of Southampton, Boldrewood Innovation Campus, Southampton, SO16 7QF, UK
- b Institute of Medical and Biological Engineering, School of Mechanical Engineering, University of Leeds, Woodhouse Lane, Leeds, LS2 9JT, UK
- ^c Croft Additive Manufacturing Ltd, Taylor Business Park, Risley, Warrington, Cheshire, WA3 6BL, UK
- d Coronary Research Group, Southampton University Hospitals NHS Trust, Souhtampton, SO16 6YD, UK
- ^e Faculty of Medicine, University of Southampton, 12 University Rd, Southampton, SO17 1BJ, UK
- f School of Mechanical Engineering, University of Leeds, Woodhouse Lane, Leeds, LS2 9JT, UK

ARTICLE INFO

Keywords: TAVI Fused leaflet FEA Simulation Laser powder bed fusion Additive manufacture 3D printing

ABSTRACT

Background: Transcatheter aortic valve implantation (TAVI) is experiencing continued growth as an option for the treatment of aortic stenosis. Both *in vitro* and *in silico* methods have proven reliable in assessing the performance of TAVI devices, which can be used in procedure planning and prototyping new concepts. 3D printing of TAVI frames has the potential for revolutionizing frame designs by making it possible to create more complex geometries. However, the mechanical performance of additively manufactured frames, in terms of crimping and deployment into an aortic root, needs to be verified if such frames are to provide a plausible and reliable method for benchtop testing.

Methods: Having previously established a suitable set of process parameters for laser powder bed fusion (LPBF) manufacture of TAVI frames based on the SAPIEN S3 design, the deployment of such a frame into a patient-specific, 3D printed aortic root phantom was undertaken and assessed using a high resolution CT scan of the result. In parallel, a full computational model was developed to simulate the same deployment procedure and validated against the *in vitro* study. Further, an interesting case study was setup using this approach to assess deployment of the LPBF frame into the same aortic root phantom but with two of the leaflets fused together. Results: The LPBF-manufactured frame had sufficient radial strength to fully open the leaflets within the aortic root phantom and anchor the frame in place for both fused and non-fused leaflet cases. There was good agreement between the *in vitro* and *in silico* tests in terms of frame position with an average nodal position error of 0.37 mm and 1.29 mm for non-fused and fused cases respectively. Similarly, the frame diameter difference between the *in vitro* and *in silico* deployments were 1.01% for the non-fused and 3.17% for the fused cases. Conclusion: Manufacture of a SAPIEN S3 type heart valve frame using LPBF has been shown to provide a viable procedure for producing frames for testing and assessment when crimped and deployed into a model of an aortic root. Further, the validated *in silico* model developed in this study can be used to computationally design and test novel frame concepts to be manufactured by LPBF.

1. Introduction

Aortic stenosis (AS) is one of the most common forms of heart disease, in which the aortic valve leaflets fail to open and close normally [1,2]. Currently, the two treatment options for AS are (i) surgical aortic valve replacement (SAVR), where the aortic valve leaflets are removed and replaced with a mechanical valve or a biological tissue valve through open-heart surgery, and (ii) the minimally invasive method

of transcatheter aortic valve implantation (TAVI), where a prosthetic valve is deployed within the patient's aortic valve via a catheter [3]. Recently, TAVI has been increasingly preferred as a treatment option over SAVR, even in younger and lower-risk patients, with the annual number of TAVI procedures overtaking the number of SAVR operations in the US in 2019 [4]. With this trend expected to continue, there is increased focus on improving TAVI outcomes, particularly in terms of new device designs, procedural guidelines, and pre-procedural planning [5].

E-mail address: o.c.eren@leeds.ac.uk (O.C. Eren).

^{*} Corresponding author.

1.1. Predicting the outcomes of TAVI procedures

In order to improve the TAVI procedure, computational simulations, especially patient-specific simulations, are increasingly used in the literature to predict the outcomes of TAVI [6]. For example, Morganti et al. simulated two TAVI deployments within an aortic root model segmented from patient scans and compared the results against postoperative echocardiography data for the same patients, finding good agreement between them in terms of geometrical changes and paravalvular leakage (PVL) [7]. Further, Schultz et al. reported a larger scale study (N = 69) of patient-specific, imaged-based simulations to predict the valve morphology and calcium displacement after the TAVI procedure, where they validated their results against computed tomography (CT) scans performed shortly after TAVI and reported a frame diameter difference of less than 1.1 mm [8]. In addition, Bosi et al. set up a patient-specific computational framework to predict outcomes of TAVI in 28 patients and reported good agreement compared to the post-procedural data, with an overall frame diameter difference of 2.6% and correct identification of PVL in 83% of all cases [9]. Besides the in silico simulation of TAVI, in vitro experiments have been used to predict TAVI outcomes, as well. For example, Qian et al. performed benchtop TAVI procedures with a CoreValve system deployed into 3D printed aortic root phantoms, which were modelled based on 18 patients who underwent TAVI, and was able to predict PVL with an accuracy of 75% [10]. The above studies demonstrate that in silico and in vitro methods are both reliable tools for assessing the performance of TAVI devices and predicting the outcomes of deployment scenarios.

1.2. Laser powder bed fusion (LPBF)

Apart from the use of computational tools to refine procedural guidelines, new valve models can greatly contribute to improving TAVI outcomes. Investigating the use of novel manufacturing methods, such as additive manufacturing, for heart valve frames can support the generation of new designs. One such method is laser powder bed fusion (LPBF) which produces complex parts by applying a powerful laser beam to selectively melt thin layers of metal powder in a layer-bylayer fashion according to the slice information of a three-dimensional model [11]. Compared with the conventional laser cutting process used to manufacture most heart valve frames, LPBF could offer high geometrical complexity to widen the design possibilities of novel heart valve concepts. Several studies have reported the feasibility of manufacturing thin strut structures via LPBF, such as stents and heart valve frames [12-14]. However, the potential performance of heart valve frames manufactured through LBPF is still unclear since LPBF parts have significant differences in microstructure, mechanical properties, and surface characteristics compared with traditionally manufactured materials [15]. Assessing the performance of LBPF-manufactured valve frames can potentially have a huge impact for the development of more complex, novel heart valve frame designs with improved clinical performance.

1.3. Bicuspid aortic valve (BAV)

In developing new valve designs and refining procedural guidelines, challenging anatomical features that can impact TAVI outcomes must be considered. One such feature is a bicuspid aortic valve (BAV) which is a congenital heart disease, occurring in 0.5%–2% of the population, and refers to the functional presence of two leaflets within the aortic valve instead of three [16]. BAV is widely recognized as a frequent cause of aortic stenosis and aortic regurgitation, with 10% of patients treated by TAVI having BAV, a considerably higher percentage compared to the overall population [17]. There are three types of BAV recognized in the literature: (i) the fused type, (ii) the 2-sinus type, and (iii) the partial fusion type. The fused and partial fusion types are the most common type of BAV (90%) and most frequently present as

the fusion of the left and right coronary leaflets (70%) [18,19]. Due to the prevalence of AS in BAV patients and the increased risk of TAVI complications in patients with BAV due to valve morphology, there is need for greater focus in assessing TAV outcomes within BAVs. While there have been several clinical studies of the use of TAVI in BAV patients, summarized in depth by Vincent et al. critical knowledge gaps still remain such as: (i) the anatomic features of BAV most suitable for TAVI, (ii) the optimal sizing technique, and (iii) the best implantation techniques [20]. As is the case with TAVI in tricuspid aortic valves, in silico and in vitro testing can play a big role in addressing these gaps. Patient-specific computational TAVI modelling in BAV patients is still limited in the literature but slowly increasing in number [21-25]. In particular, Dowling et al. reported their ongoing experience with patient-specific computer simulation of TAVI in BAV which has the potential to guide the most appropriate treatment modality for patients with BAV [21]. In vitro studies using 3D-printed, patient-specific aortic root models also demonstrated good potential in predicting patient outcomes [26]. Furthermore, Anam et al. have combined in silico and in vitro studies to establish a framework for using simulations and 3D printed models for pre-TAVI planning and assessing post-TAVI complications in BAV patients, evidencing the potential of such an approach [27].

The main aim of this research was to assess the *in vitro* deployment of a valve frame manufactured by LPBF and provide validation of an *in silico* framework which could be used to design and develop novel valve frames using LPBF. A test case of a patient specific aortic root was chosen to develop this framework with a 3D-printed aortic root model for the *in vitro* tests and high resolution CT scans were used instead of medical CT or echocardiography to present a more accurate comparison between *in vitro* and *in silico* tests. A secondary aim of this research was to compare the deployment of the LPBF-manufactured valve frame in fused (bicuspid) and non-fused (tricuspid) leaflets. The right and left coronary leaflets within the same patient-specific aortic root were fused together in both *in silico* and *in vitro* deployment tests, allowing us to determine the effects of leaflet fusing on TAVI deployment with no additional anatomical differences.

2. Methodology

2.1. Segmentation of the patient-specific aortic root model

The aortic root model was segmented from patient specific CT data of an 83-year-old male patient. Simpleware ScanIP (Synopsys Inc., US) was used to segment the aortic root wall, leaflets, and plaques into separate models. However, following segmentation, the leaflets were not continuous, as shown in Fig. 1a. There were also gaps between the leaflets and the aortic root wall and the model needed to be consolidated to allow the 3D printing of the aortic root. The segmented masks of the leaflets were manually closed as shown in Fig. 1b. The improved models were exported to a CAD package, Rhino 7 (McNeel & Associates, US), to generate smoother surfaces on all parts. Fig. 1c-f depicts the final models used for the 3D printing of the aortic root.

There was further need of model adaptation for the aortic root parts to be able to mesh them for simulations. The aortic root wall model (Fig. 1c), all three leaflet models, and the plaques were reconstructed in Rhino 7 by:

- 1. Defining section planes orthogonal to the models.
- 2. Extracting contour curves from the intersection of the section planes and models.
- 3. Lofting a new surface through the contour curves.

Fig. 2 depicts the reconstruction of the aortic root using the above steps. This process resulted in much smoother surfaces for all parts and prevented excessively deformed elements being produced in the mesh.

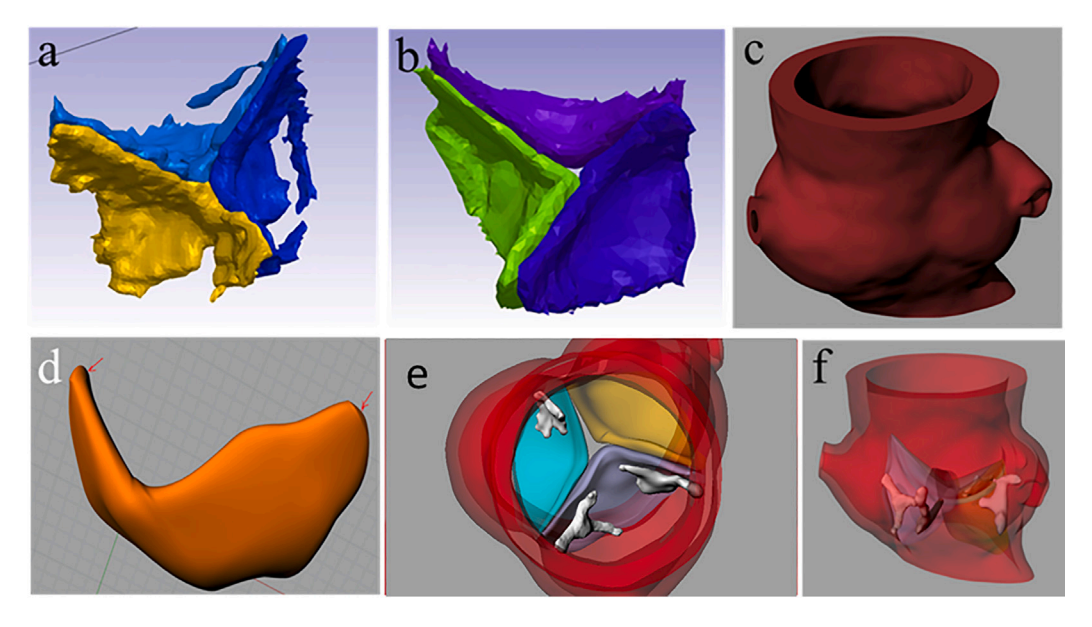


Fig. 1. (a) Auto-segmented leaflets, (b) manually segmented, gap-free leaflets in ScanIP, (c) the smoothed aortic wall model used in 3D printing, (d) one of the smoothed leaflets used in 3D printing, (e) top and (f) perspective views of the final aortic root model.

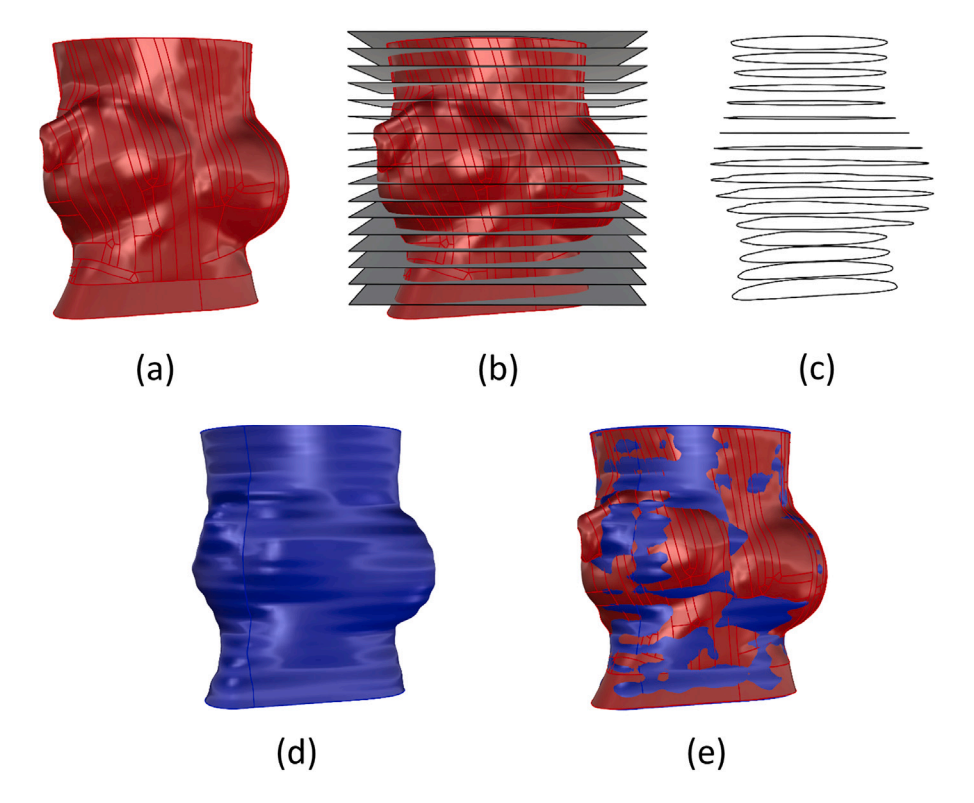


Fig. 2. (a) Initial aortic root model. (b) Section planes orthogonal to the aortic root. (c) Contour curves defining the inner surface (lumen) of the aortic root. (d) Reconstructed aortic root by lofting through the contour curves. (e) Initial aortic root model (red) overlayed on top of the reconstructed aortic root (blue).

2.2. 3D printing of the aortic root phantom

The aortic root model in Fig. 1 was sent to Stratasys (Minnesota, US) for multiple material printing. The J750 Digital Anatomy 3D Printer (Stratasys, US) was used to manufacture the aortic root phantoms. Fig. 3a shows the three material settings: soft, stiff and stiffened, as named by the manufacturer, in the print tray. Each material was a mixture of different Digital Anatomy materials from Stratasys. It was not possible to get the specific mechanical properties for the separate part materials. The material for the valve leaflets was relatively the softest while the calcified plaques' material was the most rigid. Fig. 3b

depicts the final printed aortic root phantom with the red oval showing the fused leaflets in the aortic root. The fused leaflets of one phantom were manually separated with a knife for the benchtop deployment test.

2.3. Modelling the valve frame

Balloon-expandable frames were modelled in Rhino 7 (Robert McNeel & Associates, US) and their design was based on the 26 mm SAPIEN 3 device (Edwards Lifesciences, US) which is the market leader in balloon-expandable TAVI valves. Our previous experience had

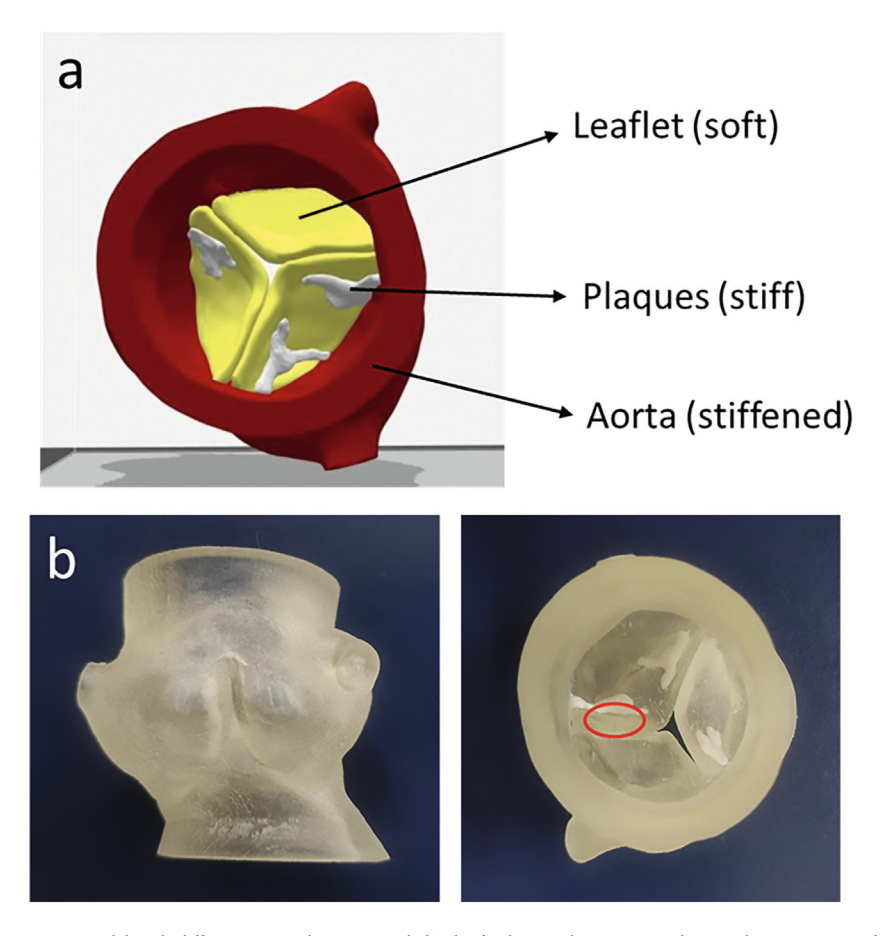


Fig. 3. (a) The sections of the aortic root model with different material settings and (b) the final printed aortic root phantom by Stratasys, with the fused leaflets shown with a red oval. The material names (soft, stiff, stiffened) are defined by Stratasys according to their material blends [28].

demonstrated that the dimensional accuracy and surface quality of the inclined struts (exemplified in Fig. 4d with a red oval) within the frame following LPBF were insufficient with the original strut angle of the frame in its expanded state [14]. Thus, the frame was modelled and manufactured in the half-crimped state (diameter of 13 mm) to improve the quality of the inclined struts. Fig. 4a–b depict the 2D sketch and 3D geometry of the half-crimped frame, respectively. The strut angle with the vertical direction was set as 19° while the strut width was 0.35 mm, as shown in Fig. 4c. The heights of the vertical struts in the bottom and top layers were 2 mm and 4 mm, as illustrated in Fig. 4d and e. The diameter of the crowns was 0.3 mm (Fig. 4d). The leaflet commissure slots had a width of 1 mm and a height of 2.95 mm (Fig. 4e). The thickness of the frame was 0.35 mm.

Prosthetic leaflets and skirt were not included within the frame model because they were assumed to have negligible impact on the deployment of the valve based on previous work within our group [29].

2.4. Laser powder bed fusion (LPBF) process

The frames were printed by Croft Additive Manufacturing (Warrington, UK) with a DiMetal-50 printer (Laseradd, China). The DiMetal-100 printer applies a 200 W fibre laser and a high-speed scan system up to 7 m/s. The building volume is 95 mm x 95 mm x 110 mm. The powder is spread by a double-cylinder one-powder feeding system. The printing process was protected in a high-purity argon gas environment. The frame was produced with a rotate hatch plus single contour strategy. The contour was scanned with 199 W and 740 mm/s. The process parameters for hatch scans were as follows: laser power of 174 W, scan speed of 998 mm/s and hatch space of 0.08 mm. The scan direction rotated by 67° between adjacent layers. The frame was placed on the

build plate with its axial direction parallel to the building direction. Thin pillars (diameter 0.3 mm, height 0.5 mm) were printed as supports to avoid damage to the frame during removal from the build plate.

The gas atomized 316L stainless steel powder used in the study was supplied by LPW Technology (Carpenter Additive, US). The powder size ranged from 10 μm to 45 μm with good flowability for powder spread. Fig. 5 shows one of the frames manufactured through the LPBF process after balloon expansion to 26 mm diameter.

2.5. In vitro benchtop deployment

The *in vitro* benchtop deployments were conducted with an Edwards Commander Delivery System (Edwards Lifesciences, US) for 26 mm frames. Fig. 6 depicts the deployment process with Fig. 6a showing the as-printed aortic root phantom and half-crimped frame. The steps of the deployment process are described below.

- In a complete TAVI device, leaflets and skirts are sutured onto the frame, something which would be almost impossible to undertake on a partially crimped frame. Thus, the half-crimped frame was firstly placed on the delivery system and expanded to full size (Fig. 6b). The outer diameter of the frame was 24.85 mm after this pre-expansion.
- The frame was crimped onto the delivery system in two steps with the Edwards THV crimper (9600 CR) as illustrated in Fig. 6c. Fig. 6d illustrates the crimped frame on the balloon, showing a dog-bone shape.
- 3. The catheter could not push through the closed leaflets within the aortic root phantom due to the friction between the yellow cone tip of the delivery system and the leaflets. Thus, the leaflets were manually opened during the catheter delivery. Fig. 6e and f

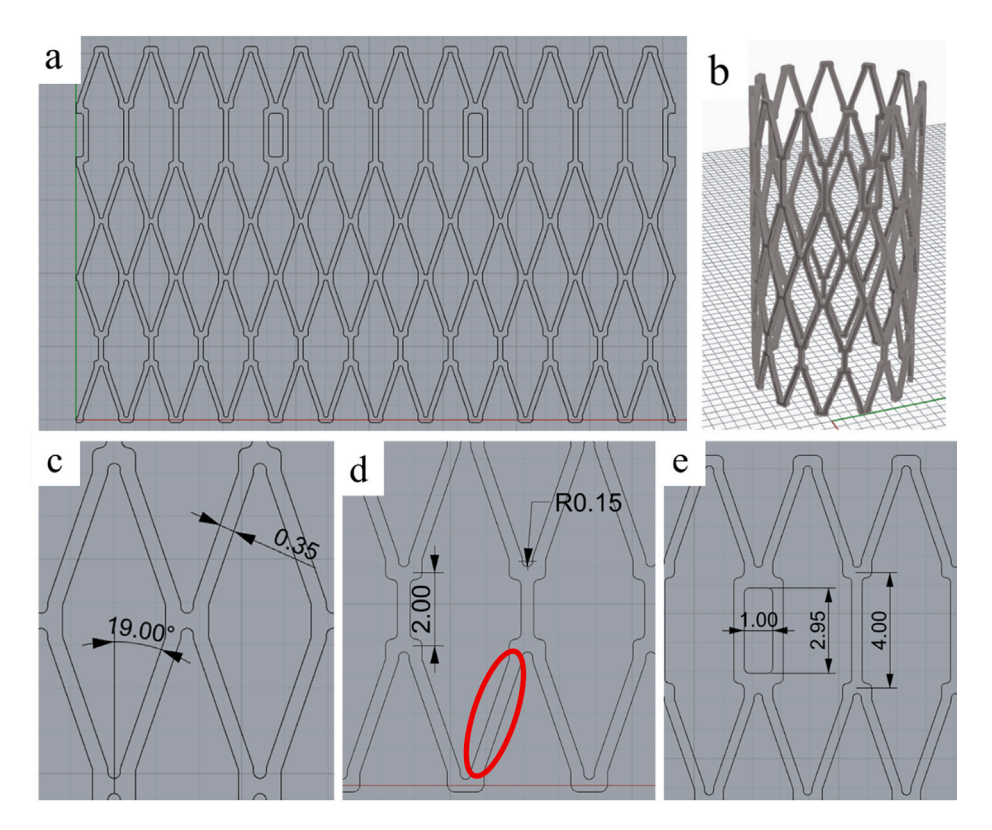


Fig. 4. (a) 2D sketch of the half-crimped frame based on Sapien 3. (b) 3D model of the frame. (c) Close-up view of the frame cells annotating the inclined strut angle and strut width. (d) Close-up view of the frame cells annotating the bottom vertical strut height and crown radius. The red oval shows one of the inclined struts for reference. (e) Close-up view of a commissure slot and top vertical strut with dimensions labelled.



 $\textbf{Fig. 5.} \ \ \textbf{The expanded frame manufactured by laser powder bed fusion}.$

show the side and top view of the frame delivered into the aortic root phantom, respectively.

4. The frame was expanded within the aortic root phantom with a water pressure between 45–70 psi (0.3–0.4 MPa) to inflate the balloon. The frame was fully opened in the aortic root as shown in Fig. 6g.

The *in vitro* deployment was performed within two aortic roots in total, one with fused leaflets and one with non-fused leaflets.

2.6. High resolution X-ray CT and segmentation of the deployed frame in the aortic root phantom

The aortic root phantoms with deployed frames were scanned by a custom Nikon XTEK XTH 225 kVp micro-focus CT system (Nikon Metrology NV, Belgium) in the μ -VIS lab at the University of Southampton. The beam voltage was set as 200 kV while the current was 115 μ A. 3142 projections were taken through 360 degrees with an exposure of 177 ms. The voxel resolution was 16 μ m. The Avizo software (Thermo Fisher Scientific, US) was used to segment and reconstruct the frames.

2.7. In silico deployment

The Abaqus/Explicit solver was used for all simulations due to its ability to analyse large, nonlinear and quasi-static cases with complex contact interactions. The FEA simulations were conducted with Abaqus/Explicit R2022 (Dassault Systemes, France) on the University of Leeds ARC4 high performance computing cluster. 8-way parallel partitioning of the complete simulation domain was employed in all simulations with 2.0 GHz Intel Xeon Gold 6138 CPUs. All simulations were solved with double precision.

2.7.1. The frame model

The frame was meshed using linear hexahedral elements (C3D8R) with reduced integration, second-order accuracy and enhanced hourglass control. The target element size was 0.12 mm resulting in a total of 81,474 elements. An image of the meshed frame model is provided in Supplementary Material (Figure S1). The mesh resolution for the frame was based on previous mesh resolution studies across several research groups, including our own, which concluded that three elements across the frame struts in the radial direction ensured mesh independence [29–31]. The mechanical properties were based on the LPBF 316L stainless steel from Croft AM and are listed in Table 1. Fig. 7 plots the true

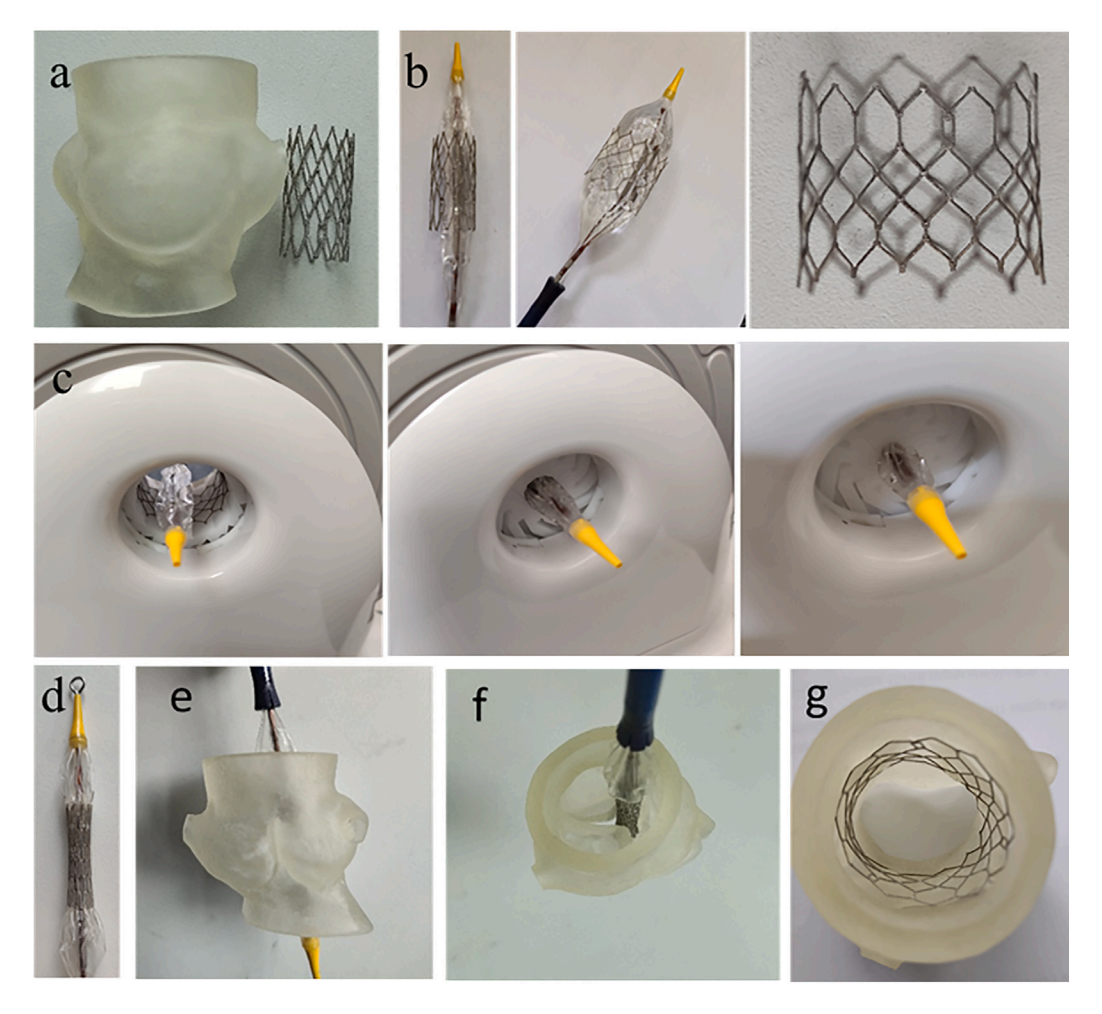


Fig. 6. The benchtop deployment procedure of the half-crimped frame in the aortic root phantom. (a) The as-printed aortic root phantom and frame. (b) the expansion of the half-crimped frame to full diameter. (c) The crimping of the frame onto the catheter. (d) The frame fully crimped onto the catheter. (e) Side and (f) axial view of the aortic root during deployment. (g) Deployed frame inside the aortic root phantom.

Table 1

Material properties for the valve frame, based on the LPBF 316L stainless steel from Croft AM.

Density	Young's modulus	Poisson's ratio	Yield stress
7.9 g/cm ³	132.5 GPa	0.3	402 MPa

strain–stress curve for the plastic stage of this material based on 3950 data points gathered by Croft AM through experimental testing. These data points were input into the material definition in Abaqus and defined the stress–strain relationship of the material beyond its yield stress.

2.7.2. The aortic root model

The aortic root model consisted of the aorta, leaflets, and plaques. All parts were meshed with quadratic tetrahedral elements (C3D10M). The aortic root was meshed with a target element size of 1 mm, resulting in 142,568 elements (Figure S2). The three leaflets — right-coronary, non-coronary, left-coronary — were meshed with a target element size of 0.5 mm, resulting in 27,843, 36,358, 24,464 elements, respectively (Figure S3).

The plaque on the non-coronary leaflet was omitted from the simulations due to excessively distorted elements forming during the meshing process even with different meshing formulations and several attempts at reconstruction. The two plaques on the right-coronary leaflet were meshed with a target element size of 0.5 mm resulting in 11,011 and 1100 elements (Figure S3).

Table 2
Material properties for the aorta and plaques.

Part	Density	Young's modulus	Poisson's ratio
Aorta [35]	1.1 g/cm ³	2 MPa	0.45
Plaque [7,34]	2 g/cm ³	12.6 MPa	0.35

Aortic plaques are composed of an irregular matrix of fibrous soft tissue and calcified masses, and, as a result, they are highly nonlinear, anisotropic and inhomogeneous [32]. The composition of each unique plaque determines its material properties and mechanical testing would be needed to accurately model them, which was not possible in this study. However, the plaque behaviour is relatively simple during valve frame deployment in that they tend to behave as large, rigid, and near unmovable masses which can be accurately captured with a linear elastic model [7,33,34]. Similarly, the valve frame predominantly interacts with the aortic leaflets rather than the aortic wall, so a linear elastic model was found sufficient to model the aorta [35]. The material properties used in the linear elastic model defining the plaques and the aorta are listed in Table 2.

The leaflets were modelled as hyperelastic with a density of 1.1 g/cm³. This material model was based on work done by Morganti et al. who fitted a nearly incompressible, reduced polynomial hyperelastic material model to experimental data from biaxial testing of human aortic tissue reported by Martin et al. [7,36]. Briefly, this reduced

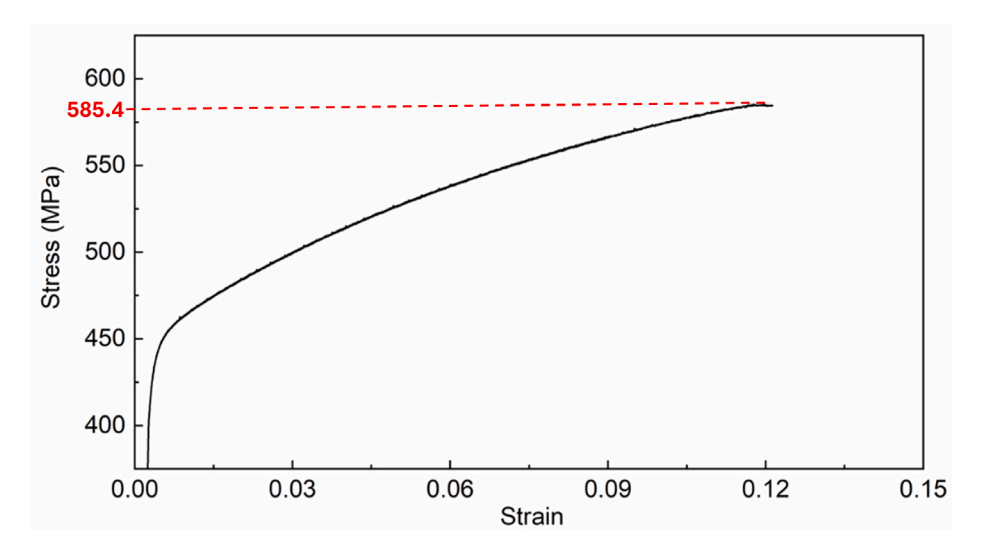


Fig. 7. True strain-stress curve of the plastic stage of the frame material based on Croft AM 316L stainless steel samples. The ultimate tensile strength of the material, 585.4 MPa, is annotated on the image.

Table 3 Reduced polynomial hyperelastic material parameters (kPa) for the leaflets [7].

Part	C10	C20	C30	C40	C50	C60
Left-coronary leaflet	23.46	1010	2110	607.8	674.3	679.9
Non-coronary leaflet	18.01	1690	1950	994.1	1490	301.5
Right-coronary leaflet	0.11	758.2	941	895.7	1040	752.8

polynomial strain energy potential (Ψ) is of the form:

$$\Psi = \sum_{i=1}^{N} C_{i0} (\bar{I}_1 - 3)^i, \tag{1}$$

where N and C_{i0} are material parameters and $\bar{I_1}$ is the first deviatoric strain invariant. $\bar{I_1}$ is defined as:

$$\bar{I}_1 = \bar{\lambda}_1^2 + \bar{\lambda}_2^2 + \bar{\lambda}_3^2,\tag{2}$$

The deviatoric stretches, $\bar{\lambda_k}$, are defined as $\bar{\lambda_k} = J^{\frac{-1}{3\lambda_k}}$ where J is the total volume ratio and λ_k are the principal stretches. Morganti et al. used a sixth-order polynomial (N = 6) and found the unknown material constants, C_{i0} , by fitting to the experimental data, resulting in the parameters listed in Table 3, which were used in this study to define the leaflet material.

Surface-to-surface tie constraints were setup between all three leaflets and the inner surface of the aortic root. Further tie constraints were defined between the non-coronary leaflet surface and the surfaces of the two plaque parts.

2.7.3. Delivery system model

The balloon catheter model was based on previous work done in our group and consisted of three parts: (i) the cone, (ii) the balloon and (iii) the guide wire [29]. A surface-to-surface tie constraint was defined between the cone and the balloon, and the guide wire was positioned in the centre of the cone. The material used to model the balloon was based on polyethylene terephthalate: Young's modulus = 1000 MPa, Poisson's ratio = 0.3, Rayleigh damping factor coefficient α = 1100 and density = 1.1 g/cm³. The same material was also assigned to the cone and the guide wire. The balloon, cone, and guide wire were meshed with triangular shell elements (S3R) resulting in 309,760, 6608, 43,200 elements, respectively (Figure S5).

2.7.4. Crimping cylinder

A radially constricting cylindrical surface was used to simulate the crimping of the frame which mimicked the crimping process of the *in vitro* tests where the crimping tool applied a radially inward force on

the frame. The cylindrical surface had an initial diameter of 28 mm and a height of 38 mm. It was meshed to 1450 linear quadrilateral surface elements (SFM3D4R) with a target element size of 1.5 mm (Figure S4). The density was 8.4 g/cm³.

2.7.5. Simulation assembly and steps

Reflecting the *in vitro* deployments, two deployment simulations were performed into an aortic root model with (i) non-fused leaflets, and (ii) fused leaflets. The assembly of both simulations comprised the same parts: catheter, aortic root, native leaflets, plaques, frame, and crimping cylinder and is shown in Fig. 8a.

The simulation steps were:

- 1. Crimping (Fig. 8b): The half-crimped frame model was fully crimped onto the balloon-catheter model via the crimping cylinder. The time period of this step was 0.1~s with a target time increment of 2E-7~s.
- 2. Leaflet opening (Fig. 8c): A pressure load was defined on the ventricular face of the leaflets to push them into an open position. The time period was 0.05 s with a target time increment of 1E-7 s.
- 3. Expansion: The balloon model was inflated to expand the frame in the first half of this step (Fig. 8d). In the second half of the step, the balloon was deflated to allow the frame to recoil (Fig. 8e). The time period was 0.1 s with a target time increment of 1E-7 s.

2.7.6. Interactions

All contact definitions comprised hard contact with no friction between the parts. Self-contact was defined for all parts except the crimping cylinder. Contact was defined between all aortic root parts (leaflets, aorta, plaques) throughout the simulation. In the Crimp and Leaflet Opening steps, the frame was only allowed to contact with the crimping cylinder and the balloon. Similarly, the crimping cylinder was only allowed to contact with the frame throughout all steps. Contact was defined between the frame, balloon, and all aortic root parts for the Expand step. Uniquely for the fused-leaflet simulations, a different contact definition was defined between the left and right coronary leaflet models that prevented separation after contact, ensuring that the edges of these leaflets that came into contact would remain fused throughout the simulation.

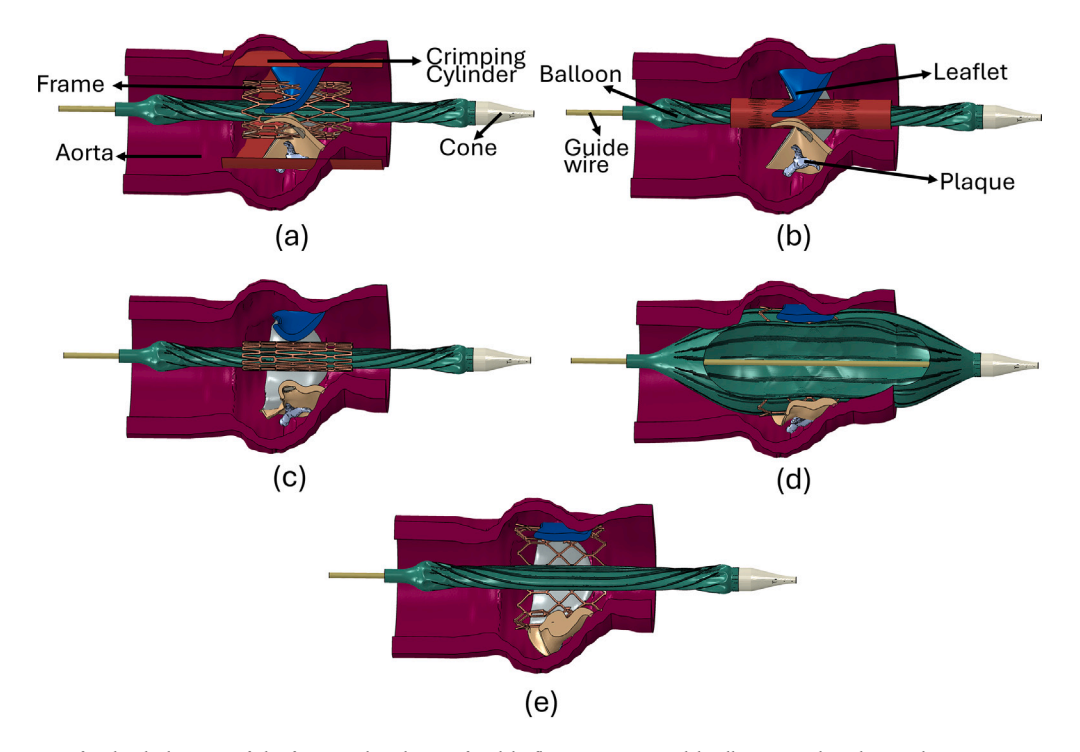


Fig. 8. The simulation steps for the deployment of the frame within the non-fused leaflet aortic root model. All parts used in the simulations are annotated on the figure. For visual clarity, a view cut was applied to all parts across a radial cross-section. (a) The initial assembly of the simulation. (b) End of the crimping step. (c) End of the leaflet opening step. The crimping cylinder was removed from in this and subsequent images for visual clarity. (d) Halfway through the Expand step with the balloon fully expanded. (e) End of the Expand step following balloon deflation.

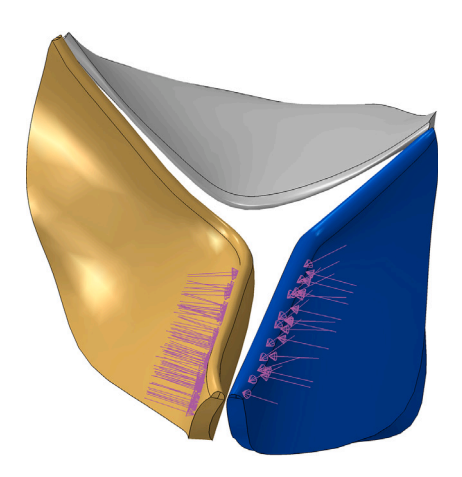


Fig. 9. The right-coronary (gold), left-coronary (blue), and non-coronary (grey) leaflets. The purple arrows show the locations of the pressure loads applied to fuse the right and left coronary leaflets.

2.7.7. Loads & boundary conditions

Two pressure loads were applied on the parts throughout both the fused and non-fused leaflet simulations. In the Leaflet Opening step, pressure loads of 2 kPa were defined on the ventricular face of all three leaflets to push them into an open position which was then deactivated in the Expand step. In the Expansion step a pressure load increasing to a maximum of 0.2 MPa was applied to the inner surface of the balloon model to inflate it and expand the frame. This pressure load was then decreased to 0 MPa in the second half of the step to deflate the balloon. For the fused leaflet case, additional pressure loads of 6 kPa were defined on the corresponding edges of the right and left coronary leaflets to push them into contact. The locations of these loads are shown in Fig. 9.

A "pinned" boundary condition was defined on the end surfaces of the aortic root, the cone, the guide wire, and the distal end of the balloon to prevent movement in all axes in all steps. A 10.5 mm displacement boundary condition in the radially inward direction was defined on the crimping cylinder during the Crimp step followed by a 0 mm displacement boundary condition throughout the next two steps.

3. Results

3.1. In vitro deployment

Fig. 10 depicts the results of the *in vitro* deployment tests. Fig. 10a is the axial view of the deployment into the non-fused leaflet case from the aortic side. The radial strength of the frame was sufficient to fully open the leaflets and anchor the frame in place. No visible damage to the frame struts occurred.

Fig. 10b and c show the deployment into the fused leaflet case, from the aortic and ventricular sides respectively. The radial strength of the frame was again sufficient to open the leaflets and anchor the frame within the aortic phantom. The fused leaflets were not split as a result of the expansion of the frame, as highlighted by the red oval in Fig. 10b. One strut close to the crowns on the ventricular side of the frame was fractured during deployment, illustrated with a red arrow in Fig. 10c. However, this fracture did not compromise the radial strength of the frame as it did not hinder opening of the leaflets.

3.2. Reconstructed 3D models

Following the *in vitro* deployments, the aortic root phantoms were scanned using high-resolution CT. Fig. 11 depicts the reconstructed 3D models based on these scans where Fig. 11a–c show the deployment result into the aortic root phantom with non-fused leaflets while Fig. 11d–f illustrate the deployment result with fused leaflets.

In the non-fused leaflets case, a small tear between the leaflets and the aortic wall, which was not visible to the naked eye, was identified

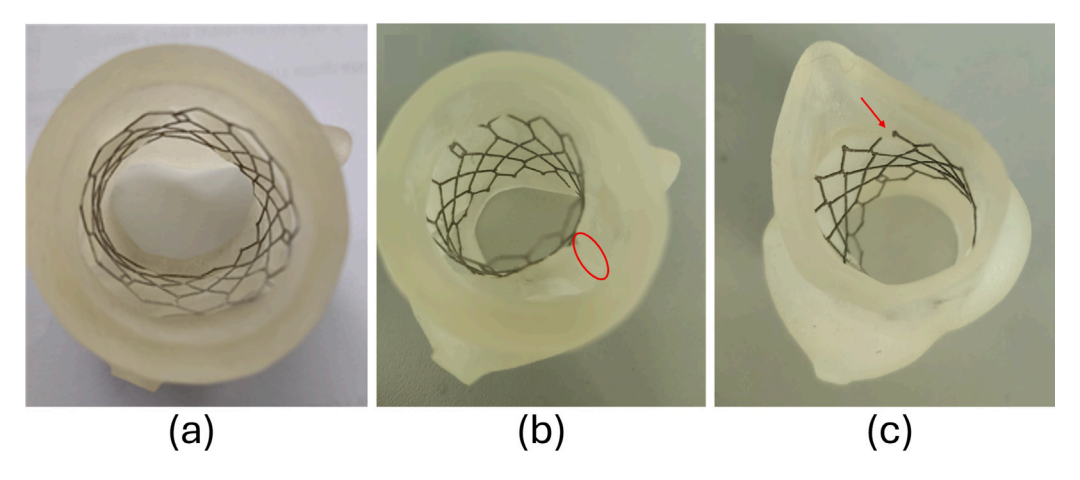


Fig. 10. The results of the *in vitro* deployments into (a) the aortic root phantom with non-fused leaflets, and the aortic root phantom with fused leaflets from the (b) aortic side and (c) ventricular side. The red oval highlights the fused leaflets. The red arrow shows the fracture of a frame strut following deployment.

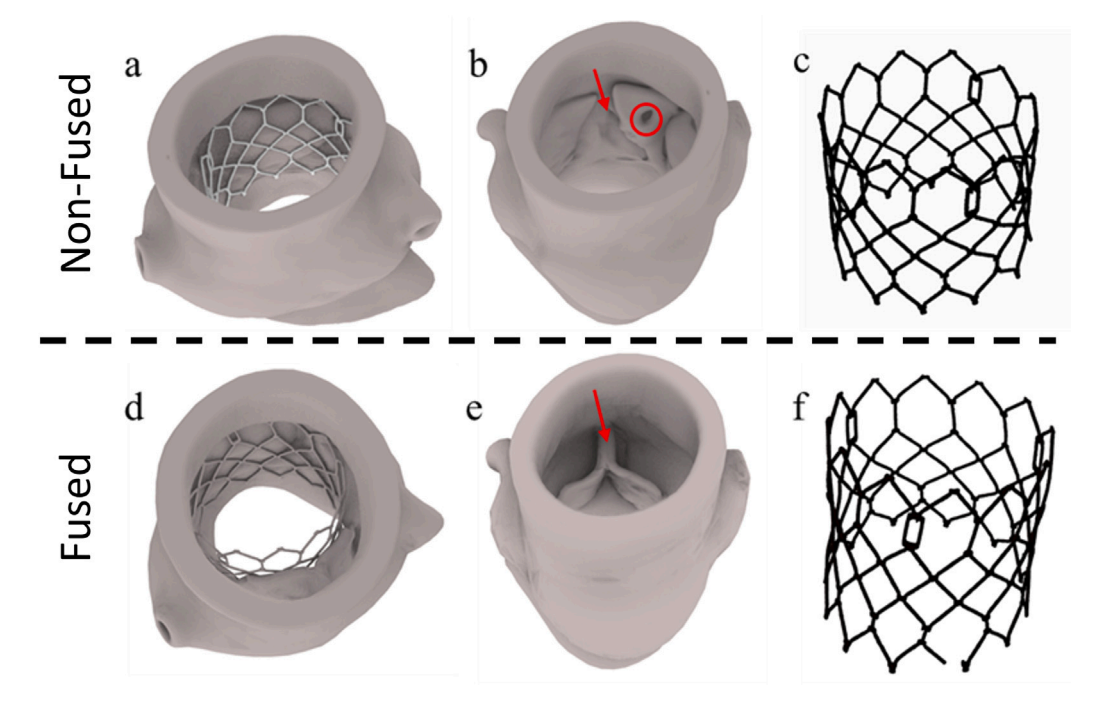


Fig. 11. Reconstructed 3D models based on the high-resolution CT scans. (a) Full assembly, (b) the aortic root, leaflets, and plaques, and (c) the frame after deployment into the aortic root phantom with non-fused leaflets. (d) Full assembly, (e) the aortic root, leaflets, and plaques, and (f) the frame after deployment into the aortic root phantom with fused leaflets.

via the CT scans, as highlighted with a red arrow in Fig. 11b. Also in Fig. 11b, the red circle shows a segmentation error that occurred due to the noise at the metal-polymer interface during CT scanning. In the fused leaflets case, the fact that the fused leaflets were not split as a result of frame deployment *in vitro* was correctly captured in the segmented model, as marked with a red arrow in Fig. 11e.

Fig. 11c and f show the frames after deployment into both aortic root phantoms. The frame was expanded to a larger diameter when deployed in the non-fused leaflets, as would be expected due to less leaflet material being present between the aortic wall and the frame. The broken strut depicted previously in Fig. 10b was captured through the high-resolution CT scans as shown in Fig. 11f.

3.3. In silico deployment

Fig. 12a shows the results of the deployment simulation into the non-fused leaflet aortic root and Fig. 12b shows the result for the fused

case. The fused leaflets remained together following deployment of the frame, emphasized with the red oval in Fig. 12b, similar to the *in vitro* tests.

The average stress profiles were nearly identical between the two cases. Figure S6 plots this average von Mises stress on the valve frames across the balloon expansion step of the simulations within both the fused and non-fused leaflets. The locations of the high stress regions on the frames across both cases were also very similar. Figure S7 shows the contour plot of von Mises stresses at the step time increment of maximum average von Mises stress, corresponding to maximum balloon inflation. The regions on the frames with the highest stress points corresponded to the crowns of the cells of the frame which were deformed the most during crimping and expansion. The maximum stress for both cases throughout the entire simulation was 585.3 MPa.

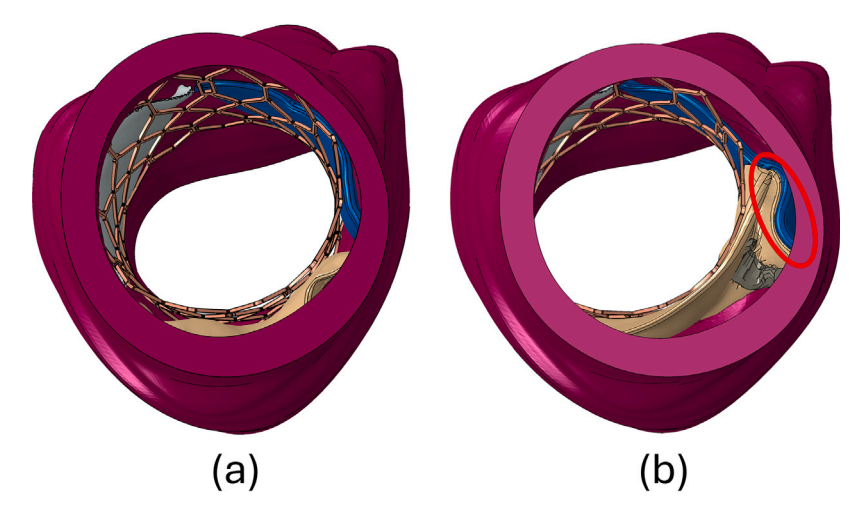


Fig. 12. Final position of the frame following the simulation of deployment into the aortic root model with (a) non-fused and (b) fused leaflets. The red oval emphasizes the fused leaflets which were still attached following deployment.

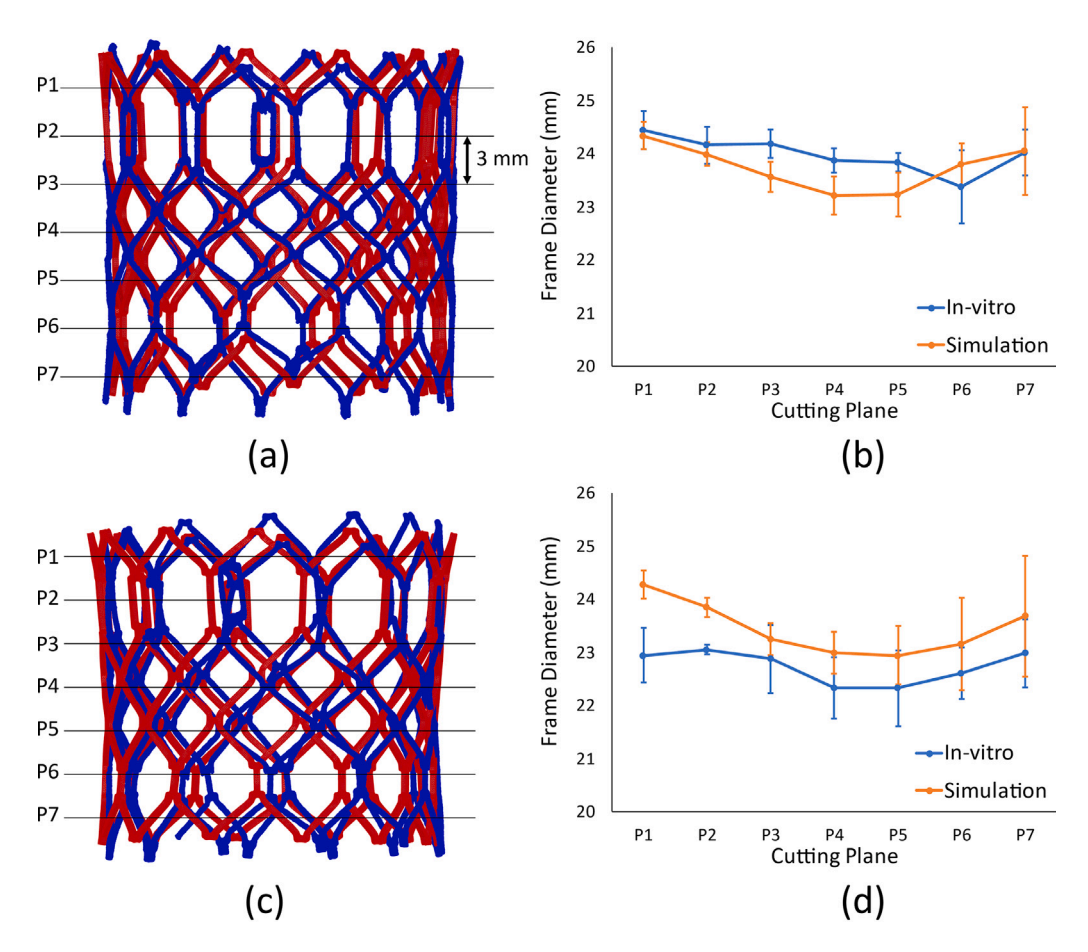


Fig. 13. (a) The frame models after deployment into the aortic root with non-fused leaflets from the *in vitro* (blue) and *in silico* (red) tests. The positions of the seven cutting planes (P1-P7) across the height of the frames and the distance between the planes are shown. (b) Plot of the diameter of the frames at each cutting plane for the *in vitro* (blue) and *in silico* (orange) deployments into the aortic root with non-fused leaflets. The error bars represent the variation of the diameter of the frames at each cutting plane. (c) The frame models after deployment into the aortic root with fused leaflets from the *in vitro* (blue) and *in silico* (red) tests. The positions of the seven cutting planes (P1-P7) are also shown. (d) Plot of the diameter of the frames at each cutting plane for the *in vitro* (blue) and *in silico* (orange) deployments into the aortic root with fused leaflets.

3.4. Comparison between the in vitro and in silico deployments

Following the *in vitro* and *in silico* deployments into fused and nonfused leaflets, the results were compared in terms of the final positions of the frames. The reconstructed 3D models from the CT scans, and the deformed aortic root and frame models from the simulations were

imported into the CAD software Rhino 7. Individually, for the fused and non-fused cases, the models were aligned and overlaid with respect to the aortic root geometries. Fig. 13a and c show the pairs of frames for both the fused and non-fused cases overlaid.

From this, the positional differences between the frames were investigated. The first method of comparing the positional difference

identified the closest node on the CT scan frame mesh for every single node on the simulated frame mesh and calculated the distance between them. For the non-fused case, the average distance between nodes was 0.37 mm and the maximum distance was 1.29 mm. For the fused case, the average and maximum distances were 0.64 mm and 2.37 mm respectively.

The second method of identifying the difference was to compare the diameter of the frames across their height. Seven cutting planes were defined equidistant across the height of each frame, as shown in Fig. 13a and c, and the diameter of the frame at each of these positions was calculated. Fig. 13b and d plot the frame diameters at the intersection of each cutting plane for the non-fused and fused cases, respectively. The overall diameter of both the simulated and physical frames were smaller when deployed within fused leaflets. Similarly, the frames within fused leaflets were more non-circular, as evidenced by the larger error bars present in most cutting planes in Fig. 13d.

4. Discussion

The main aim of this research was to evaluate the deployment of an additively manufactured TAVI frame. To the authors' knowledge this represents the first reported case of the *in vitro* deployment of a heart valve frame manufactured through laser powder bed fusion (LPBF) within a patient-specific aortic root model.

4.1. Radial strength of the frame

The LPBF-manufactured frame exhibited sufficient radial strength to open and anchor within the leaflets of the aortic root model. This was the case for both the *in vitro* tests where the manufacturer, Stratasys, stated that the materials of the aortic root phantom closely resemble that of human tissue, and the *in silico* tests where the material properties of the aortic root model reflected that of human tissue reported widely in literature [28]. Beyond this, the frame was also able to open the leaflets and anchor within the aortic root when deployed within fused leaflets, which presented a higher radial resistance. These results are promising for the future development of novel heart valve designs using LPBF in terms of achieving meaningful deployment outcomes.

The main advantage of using additive manufacturing methods such as LPBF for heart valve frames is the ability to generate more complex structures, particularly in terms of having different features located at different radial planes within the overall frame structure which is unfeasible with common subtractive manufacturing techniques. Although the results of this study is promising, there are other clinical requirements on heart valve frames beyond the mechanical aspect such as haemocompatibility and biocompatibility. In these aspects, further developments are needed to improve the surface quality of these 3D-printed frames, as discussed in an earlier article [14].

4.2. In silico design framework

Another aim of this research was to validate a computational model of the LPBF-manufactured frames for future use in designing new heart valve frames. The methodology presented in this work has achieved close agreement between the *in vitro* and *in silico* tests. A similar comparison between CT scans and simulations in the literature reported less than 1.1 mm difference between frame diameters across vertical slices, compared to our results of less than 0.67 mm for the non-fused and less than 1.33 mm for the fused cases [8]. Another study reported an overall frame diameter difference between CT scans and simulations as 2.6%, which compares well to our diameter differences of 1.01% and 3.17% for the non-fused and fused cases respectively [9]. Finally, Anam et al. reported an overall mean frame diameter difference between *in vitro* and *in silico* deployments into a patient specific aortic root with BAV of 0.40 ± 1.36 mm, compared to our findings of 0.25 ± 0.45 mm and 0.72 ± 0.61 mm for the non-fused and fused cases respectively [27]. An

important aspect in achieving such good agreement between the scans and the simulations was the use of high resolution x-ray CT scans which allowed the reconstruction of very accurate computational models of the *in vitro* tests for comparison. Thus, the methodology presented here can be used in the computational design and testing of new heart valve designs prior to manufacturing by LPBF.

Another use case for LPBF printed frames could be in validating computational studies in general. Many researchers find it difficult to acquire or manufacture TAVI devices due to associated high costs and hence cannot validate their computational models fully. Using LPBF to manufacture their models could be a low cost option for running *in vitro* tests and validating computational models.

4.3. Fused vs. non-fused leaflets

The patient specific aortic root used in this study anatomically had non-fused leaflets. The fused leaflet case and its comparison with the initial non-fused aortic root was chosen as a test case to determine the mechanical feasibility of the LPBF-manufactured frame, particularly because fused leaflets present a challenging anatomy in terms of the required radial force. As expected, the final diameter of the frame in both the in vitro and in silico studies was lower for the fused anatomy (mean diameter = 23.09 mm) compared to the non-fused anatomy (mean diameter = 23.87 mm). This difference was particularly pronounced between cutting planes P4 and P5, as can be seen in Fig. 13. This comparison appears to be unique in the literature because it captured the difference that fused leaflets caused for the deployment of a TAVI frame while all other anatomical aspects were the same. The decreased diameter of the frame in the fused leaflet case reinforces the focus needed on the treatment of aortic stenosis in BAV patients, whether through lacerating the fused leaflets prior to valve implantation or designing new valves specific to the challenges posed by fused leaflets, to improve clinical outcomes in these patients.

The predicted stresses for the fused and non-fused cases were nearly identical, both in terms of magnitude and profile across the step time, suggesting that the presence of the fused leaflets did not produce additional strain on the frames and that the stresses on the frames were dominated by the interaction between the balloon and the frames. The fracture present in the in vitro deployment into the fused leaflets was within the regions of high stresses predicted in the in silico tests, namely on the bottom crowns of the frame. However, this fracture may well have occurred when detaching the 3D-printed material from the build plate rather than during in vitro deployment. The yield stress of the material was exceeded across both frames, which was expected and necessary since balloon-expanding valve frames must undergo plastic deformation to expand during deployment. Some regions of the frame underwent stresses within 5% of the ultimate tensile strength of the material and the maximum predicted stress for both cases was 585.3 MPa. While the computational model did not include fracturing, breakages could occur in these regions in vitro. Indeed, this is one of the reasons that higher strength alloys, such as Cobalt-Chromium, are used in industry rather than stainless steel for balloon-expanding prosthetic heart valve frames. While 316L stainless steel was used in this research due to manufacturing constraints, the developed computational framework will apply for other materials through substituting the associated material model parameters.

4.4. Limitations

In common with other TAVI deployment simulations, results are dependent on multiple modelling assumptions. These include the omission of the leaflets and skirt within the frame model which may impact the deployment of the valve, although this omission was justified in previous work [29]. The material properties used for the aortic root parts (aorta, leaflets, plaque) were not based on the material properties of the 3D-printed aortic root phantom as these were not made available by the

manufacturer. However, it is noted that material property models are generally approximate. Also, the way constraints and other boundary conditions are defined for securing the leaflets to the aortic root could have an impact, particularly on the stresses around the aorta-leaflet attachment lines. Further, the contact between the parts was defined as frictionless and the hard contact pressure-overclosure relationship was used. In this contact model the surfaces do not transmit any contact pressure until there is contact between them (i.e. until the clearance between them is zero). The magnitude of contact pressure transmission is limitless when the surfaces are in contact, which may have produced artificially large stresses on the contact surfaces between the frame, crimping cylinder, leaflets, and aorta. However, the hard contact relationship minimizes the penetration between the surfaces in contact which is why this contact method was used.

Additional uncertainties include the segmentation of the aortic root parts prior to the 3D printing of the phantom. In particular, the leaflet models had to be manually adjusted to generate smooth enough parts for 3D printing which could have compromised their accuracy. Further reconstruction of these models was necessary for the computational simulations as well, which could have contributed to the discrepancy between the *in vitro* and simulation outcomes. Moreover, the pressure load defined to inflate the balloon in the *in silico* simulations, 0.2 MPa, was lower than the pressure used in the *in vitro* tests, 0.3–0.4 MPa, due to greater pressure load values causing computational errors, which may have influenced the results. Finally, one plaque which was present in the aortic root phantom could not be included in the computational simulations.

It is also important to note that neither the *in vitro* nor the *in silico* tests included the effects of blood flow on the valve frame. In designing a frame, the shear stresses generated by blood flow and potential platelet activation that could result from the device design should also be considered alongside the radial wall interactions captured in this study.

Despite the limitations detailed above, evidence from the research reported in this article shows that LPBF-manufactured frames have sufficient radial strength to be used in TAVI devices and presents a validated computational method for simulating the behaviour of these frames, providing interesting insight and useful guidance for future development in 3D printed heart valve frames.

5. Conclusion

In conclusion, this study presented the successful deployment of LPBF-manufactured frames into 3D printed patient-specific aortic root phantoms with fused and non-fused valve leaflets, evidencing their suitability for testing and/or assessing the performance of prosthetic heart valve frames, albeit with the omission of prosthetic leaflets and skirt. These *in vitro* deployments were computationally reconstructed via high resolution CT scans and compared against *in silico* deployments of the same scenarios, showing good agreement. Through this validation, these *in silico* models can be used in future computational development and testing of novel frames manufactured via LPBF.

CRediT authorship contribution statement

Xiao Zhao: Writing – review & editing, Writing – original draft, Visualization, Project administration, Methodology, Investigation, Data curation, Conceptualization. Oguz Can Eren: Writing – review & editing, Writing – original draft, Visualization, Software, Methodology, Investigation. Anthony Molyneux: Resources, Methodology. Louise Geekie: Resources, Methodology. Nick Curzen: Writing – review & editing, Supervision, Funding acquisition, Conceptualization. Neil W. Bressloff: Writing – review & editing, Supervision, Project administration, Methodology, Funding acquisition, Conceptualization.

Ethical approval

All procedures were performed in compliance with relevant laws and institutional guidelines. Further ethical approval not required.

Funding

This work was supported by the Engineering and Physical Sciences Research Council (EPSRC, UK), [Grant No. EP/S030182/1]. For the purpose of open access, the author has applied a Creative Commons Attribution (CC BY) licence to any Author Accepted Manuscript version arising from this submission.

Declaration of competing interest

The authors declare the following financial interests/personal relationships which may be considered as potential competing interests: Curzen is involved in unrestricted research grants from Boston Scientific, HeartFlow and Beckman Coulter and receives speaker/consultancy fees from Boston Scientific, HeartFlow and Abbott. The other authors have no competing interests to report.

Acknowledgements

This work was undertaken on ARC4, part of the High Performance Computing facilities at the University of Leeds, UK.

Appendix A. Supplementary data

Supplementary material related to this article can be found online at https://doi.org/10.1016/j.compbiomed.2025.109690.

References

- R.O. Bonow, P. Greenland, Population-wide trends in aortic stenosis incidence and outcomes, Circ. 131 (11) (2015) 969–971, http://dx.doi.org/10.1161/ circulationaha.115.014846.
- [2] K. Maganti, V.H. Rigolin, M.E. Sarano, R.O. Bonow, Valvular heart disease: Diagnosis and management, Mayo Clin. Proc. 85 (5) (2010) 483–500, http://dx.doi.org/10.4065/mcp.2009.0706.
- [3] A. Cribier, H. Eltchaninoff, A. Bash, N. Borenstein, C. Tron, F. Bauer, G. Derumeaux, F. Anselme, F. Laborde, M.B. Leon, Percutaneous transcatheter implantation of an aortic valve prosthesis for calcific aortic stenosis First human case description, Circ. 106 (24) (2002) 3006–3008, http://dx.doi.org/10.1161/01.cir.0000047200.36165.B8.
- [4] J.D. Carroll, M.J. Mack, S. Vemulapalli, H.C. Herrmann, T.G. Gleason, G. Hanzel, G.M. Deeb, V.H. Thourani, D.J. Cohen, N. Desai, A.J. Kirtane, S. Fitzgerald, J. Michaels, C. Krohn, F.A. Masoudi, R.G. Brindis, J.E. Bavaria, STS-ACC TVT registry of transcatheter aortic valve replacement, Am. J. Cardiol. 76 (21) (2020) 2492–2516, http://dx.doi.org/10.1016/j.jacc.2020.09.595.
- [5] E. Cerrato, L. Nombela-Franco, T.M. Nazif, H. Eltchaninoff, L. Søndergaard, H.B. Ribeiro, M. Barbanti, F. Nietlispach, P.D. Jaegere, P. Agostoni, R. Trillo, P. Jimenez-Quevedo, F. D'Ascenzo, O. Wendler, G. Maluenda, M. Chen, C. Tamburino, C. Macaya, M.B. Leon, J. Rodes-Cabau, Evaluation of current practices in transcatheter aortic valve implantation: The written (worldwide tavi experience) survey, Int. J. Cardiol. 228 (2017) 640–647, http://dx.doi.org/10. 1016/j.ijcard.2016.11.104.
- [6] P. Vy, V. Auffret, P. Badel, M. Rochette, H.L. Breton, P. Haigron, S. Avril, Review of patient-specific simulations of transcatheter aortic valve implantation, Int. J. Adv. Eng. Sci. Appl. Math. 8 (2016) 2–24, http://dx.doi.org/10.1007/s12572-015-0139-9.
- [7] S. Morganti, M. Conti, M. Aiello, A. Valentini, A. Mazzola, A. Reali, F. Auricchio, Simulation of transcatheter aortic valve implantation through patient-specific finite element analysis: Two clinical cases, J. Biomech. 47 (11) (2014) 2547–2555, http://dx.doi.org/10.1016/j.jbiomech.2014.06.007.
- [8] C. Schultz, R. Rodriguez-Olivares, J. Bosmans, T. Lefèvre, G. De Santis, N. Bruining, T.D. V. Collas, B. Bosmans, Z. Rahhab, Patient-specific image-based computer simulation for theprediction of valve morphology and calcium displacement after TAVI with the Medtronic CoreValve and the Edwards SAPIEN valve, Eurointervention 11 (9) (2016) 1044–1052, http://dx.doi.org/10.4244/ELJV1119A212.

- [9] G.M. Bosi, C. Capelli, M.H. Cheang, N. Delahunty, M. Mullen, A.M. Taylor, S. Schievano, A validated computational framework to predict outcomes in TAVI, Sci. Rep. 10 (2020) 9906, http://dx.doi.org/10.1038/s41598-020-66899-6.
- [10] Z. Qian, K. Wang, S.Z. Liu, X. Zhou, V. Rajagopal, C. Meduri, J.R. Kauten, Y.H. Chang, C.S. Wu, C. Zhang, B. Wang, M.A. Vannan, Quantitative prediction of paravalvular leak in transcatheter aortic valve replacement based on tissue-mimicking 3D printing, JACC Cardiovasc. Imaging 10 (7) (2017) 719–731, http://dx.doi.org/10.1016/j.jcmg.2017.04.005.
- [11] D. Wang, Y.Q. Yang, R.C. Liu, D.M. Xiao, J.F. Sun, Study on the designing rules and processability of porous structure based on selective laser melting (SLM), J. Mater. Process. Tech. 213 (10) (2013) 1734–1742, http://dx.doi.org/10.1016/j. imatprotec.2013.05.001.
- [12] S.G. Choi, S.H. Kim, W.K. Choi, E. Lee, The optimum condition selection of electrochemical polishing and surface analysis of the stainless steel 316L by the Taguchi method, Int. J. Adv. Manuf. Technol. 82 (2016) 1933–1939, http: //dx.doi.org/10.1007/s00170-015-7404-8.
- [13] H. Zhao, J. Van Humbeeck, J. Sohier, I. De Scheerder, Electrochemical polishing of 316L stainless steel slotted tube coronary stents, J. Mater. Sci. Mater. Med. 13 (10) (2002) 911–916, http://dx.doi.org/10.1023/a:1019831808503.
- [14] X. Zhao, A. Liang, M. Bellin, N.W. Bressloff, Effects of process parameters and geometry on dimensional accuracy and surface quality of thin strut heart valve frames manufactured by laser powder bed fusion, Int. J. Adv. Manuf. Technol. 133 (2024) 543–557, http://dx.doi.org/10.1007/s00170-024-13627-3.
- [15] B. Song, X. Zhao, S. Li, C. Han, Q. Wei, S. Wen, J. Liu, Y. Shi, Differences in microstructure and properties between selective laser melting and traditional manufacturing for fabrication of metal parts: A review, Front. Mech. Eng. 10 (2015) 111–125, http://dx.doi.org/10.1007/s11465-015-0341-2.
- [16] D. Tchetche, C. de Biase, L. van Gils, R. Parma, A. Ochala, T. Lefevre, T. Hovasse, O.D. Backer, L. Sondergaard, S. Bleiziffer, R. Lange, R. Kornowski, U. Landes, B.L. Norgaard, L. Biasco, R. Philippart, J.M.-M. de Nicolas, D. Mylotte, C. Lemee, N. Dumonteil, N.M. Van Mieghem, Bicuspid aortic valve anatomy and relationship with devices: The bavard multicenter registry, Circ. Cardiovasc. Interv. 12 (1) (2019) e007107, http://dx.doi.org/10.1161/CIRCINTERVENTIONS.118.007107.
- [17] W.-K. Kim, C. Liebetrau, U. Fischer-Rasokat, M. Renker, A. Rolf, M. Doss, H. Möllmann, H. Nef, T. Walther, C.W. Hamm, Challenges of recognizing bicuspid aortic valve in elderly patients undergoing TAVR, Int. J. Cardiovasc. Imaging 36 (2) (2020) 251–256, http://dx.doi.org/10.1007/s10554-019-01704-8.
- [18] H.I. Michelena, A.D. Corte, A. Evangelista, J.J. Maleszewski, W.D. Edwardsa, M.J. Romana, R.B. Devereux, B. Fernández, F.M. Asch, A.J. Barker, L.M. Sierra-Galan, L. De Kerchove, S.M. Fernandes, P.W.M. Fedak, E. Girdauskas, V. Delgado, S. Abbara, E. Lansac, S.K. Prakash, M.M. Bissell, B.A. Popescu, M.D. Hope, M. Sitges, V.H. Thourani, P. Pibarot, K. Chandrasekaran, P. Lancellotti, M.A. Borger, J.K. Forrest, J. Webb, D.M. Milewicz, R. Makkar, M.B. Leon, S.P. Sanders, M. Markl, V.A. Ferrari, W.C. Roberts, J.-K. Song, P. Blanke, C.S. White, S. Siu, L.G. Svensson, A.C. Braverman, J. Bavaria, T.M. Sundt, G. El Khoury, R. De Paulis, M. Enriquez-Sarano, J.J. Bax, C.M. Otto, H.-J. Schäfers, International consensus statement on nomenclature and classification of the congenital bicuspid aortic valve and its aortopathy, for clinical, surgical, interventional and research purposes, Eur. J. Cardiothorac Surg. 60 (3) (2021) 448–476, http://dx.doi.org/10.1093/ejcts/ezab038.
- [19] H.-H. Sievers, C. Schmidtke, A classification system for the bicuspid aortic valve from 304 surgical specimens, J. Thorac. Cardiovasc. Surg. 133 (5) (2007) 1226–1233, http://dx.doi.org/10.1016/j.jtcvs.2007.01.039.
- [20] F. Vincent, J. Ternacle, T. Denimal, M. Shen, B. Redfors, C. Delhaye, M. Simonato, N. Debry, B. Verdier, B. Shahim, T. Pamart, H. Spillemaeker, G. Schurtz, F. Pontana, V.H. Thourani, P. Pibarot, E.V. Belle, Transcatheter aortic valve replacement in bicuspid aortic valve stenosis, Circ. 143 (10) (2021) 1043–1061, http://dx.doi.org/10.1161/CIRCULATIONAHA.120.048048.
- [21] C. Dowling, R. Gooley, L. McCormick, R.P. Sharma, A.C. Yeung, W.F. Fearon, J. Dargan, F. Khan, S. Firoozi, S.J. Brecker, Ongoing experience with patient-specific computer simulation of transcatheter aortic valve replacement in bicuspid aortic valve, Cardiovasc. Revasc. Med. 51 (2023) 31–37, http://dx.doi. org/10.1016/j.carrev.2023.01.015.

- [22] S.B. Anam, B.J. Kovarovic, R.P. Ghosh, M. Bianchi, A. Hamdan, R. Haj-Ali, D. Bluestein, Assessment of paravalvular leak severity and thrombogenic potential in transcatheter bicuspid aortic valve replacements using patient-specific computational modeling, J. Cardiovasc. Trans. Res. 15 (2022) 834–844, http://dx.doi.org/10.1007/s12265-021-10191-z.
- [23] C. Dowling, S. Firoozi, S.J. Brecker, First-in-human experience with patient-specific computer simulation of TAVR in bicuspid aortic valve morphology, JACC Cardiovasc. Interv. 13 (2) (2020) 184–192, http://dx.doi.org/10.1016/j.jcin.2019.07.032.
- [24] K. Lavon, G. Marom, M. Bianchi, R. Halevi, A. Hamdan, A. Morany, E. Raanani, D. Bluestein, R. Haj-Ali, Biomechanical modeling of transcatheter aortic valve replacement in a stenotic bicuspid aortic valve: deployments and paravalvular leakage, Med. Biol. Eng. Comput. 57 (2019) 2129–2143, http://dx.doi.org/10. 1007/s11517-019-02012-y.
- [25] S. Pasta, S. Cannata, G. Gentile, M.D. Giuseppe, F. Cosentino, F. Pasta, V. Agnese, D. Bellavia, G.M. Raffa, M. Pilato, C. Gandolfo, Simulation study of transcatheter heart valve implantation in patients with stenotic bicuspid aortic valve, Med. Biol. Eng. Comput. 58 (2020) 815–829, http://dx.doi.org/10.1007/s11517-020-02138-4.
- [26] A.P.-W. Lee, C.W.M. Leong, K.-W. Kwok, Y. Fan, Using 3d printed models for planning transcatheter aortic valve implantation in patients with bicuspid aortic valve, J. Am. Coll. Cardiol. 71 (11) (2018) 10–12, http://dx.doi.org/10.1016/ S0735-1097(18)31671-1.
- [27] S.B. Anam, B.J. Kovarovic, R.P. Ghosh, M. Bianchi, A. Hamdan, R. Haj-Ali, D. Bluestein, Validating in silico and in vitro patient-specific structural and flow models with transcatheter bicuspid aortic valve replacement procedure, Cardiovasc. Eng. Technol. 13 (2022) 840–856, http://dx.doi.org/10.1007/s13239-022-00620-8.
- [28] Stratasys Inc., Biomechanical Tests Confirm the Potential for 3D Printing Synthetic Myocardium With the Stratasys J750 Digital Anatomy Printer, Tech. Rep., Stratasys Inc., 2020.
- [29] J. Bailey, N. Curzen, N.W. Bressloff, Assessing the impact of including leaflets in the simulation of TAVI deployment into a patient-specific aortic root, Comput. Methods Biomech. Biomed. Eng. 19 (7) (2016) 733–744, http://dx.doi.org/10. 1080/10255842.2015.1058928.
- [30] D. Carbonaro, D. Gallo, U. Morbiducci, A. Audenino, C. Chiastra, In silico biomechanical design of the metal frame of transcatheter aortic valves: multiobjective shape and cross-sectional size optimization, Struct. Multidiscip. Optim. 64 (2021) 1825–1842, http://dx.doi.org/10.1007/s00158-021-02944-w.
- [31] O.C. Eren, N. Curzen, N.W. Bressloff, Magnetic retrieval of prosthetic heart valves for redo-TAVI, Med. Eng. Phys. 101 (2022) 103761, http://dx.doi.org/10.1016/ j.medengphy.2022.103761.
- [32] G.A. Holzapfel, G. Sommer, P. Regitnig, Anisotropic mechanical properties of tissue components in human atherosclerotic plaques, J. Biomech. Eng. 126 (5) (2004) 657–665, http://dx.doi.org/10.1115/1.1800557.
- [33] C. Capelli, G.M. Bosi, E. Cerri, J. Nordmeyer, T. Odenwald, P. Bonhoeffer, F. Migliavacca, A.M. Taylor, S. Schievano, Patient-specific simulations of transcatheter aortic valve stent implantation, Med. Biol. Eng. Comput. 50 (2012) 183–192, http://dx.doi.org/10.1007/s11517-012-0864-1.
- [34] Q. Wang, S. Kodali, C. Primiano, W. Sun, Simulations of transcatheter aortic valve implantation: implications for aortic root rupture, Biomech. Model. Mechanobiol. 14 (2014) 29–38, http://dx.doi.org/10.1007/s10237-014-0583-7.
- [35] F.L. Xiong, W.A. Goetz, C.K. Chong, Y.L. Chua, S. Pfeifer, E. Wintermantel, J.H. Yeo, Finite element investigation of stentless pericardial aortic valves: relevance of leaflet geometry, Ann. Biomed. Eng. 38 (2010) 1908–1918, http://dx.doi.org/10.1007/s10439-010-9940-6.
- [36] C. Martin, T. Pham, W. Sun, Significant differences in the material properties between aged human and porcine aortic tissues, Eur. J. Cardiothorac Surg. 40 (2011) 28–34, http://dx.doi.org/10.1016/j.ejcts.2010.08.056.